Prediction of Temperature-Dependent Stress in 4H-SiC Using In Situ Nondestructive Raman Spectroscopy Characterization

Yang, Zhoudong; Wang, Xinyue; Zuo, Yuanhui; Tang, Zhuorui; Tang, Hongyu; Zhang, Rongjun; Fan, Xuejun; Zhang, Guoqi; Fan, Jiajie; More Authors

DOI
10.1002/lpor.202401033

Publication date
2024

Document Version
Final published version

Published in
Laser and Photonics Reviews

LASER & PHOTONICS REVIEWS
www.lpr-journal.org

Prediction of Temperature-Dependent Stress in 4H-SiC Using In Situ Nondestructive Raman Spectroscopy Characterization

Zhoudong Yang, Xinyue Wang, Yuanhui Zuo, Zhuorui Tang, Baotong Guo, Junran Zhang, Hongyu Tang, Rongjun Zhang,* Xuejun Fan, Guoqi Zhang, and Jiajie Fan**

4H-SiC is widely used in power electronics owing to its superior physical properties. However, temperature-induced stresses compromise the reliability of 4H-SiC power devices in high-temperature applications, warranting precise, and nondestructive stress characterization responsive to temperature variations. Herein, a temperature-dependent predictive model is proposed for analyzing the Raman shift–stress in 4H-SiC. The 4H-SiC epitaxial samples prepared via chemical vapor deposition are characterized using in situ variable-temperature Raman spectroscopy, resulting in a temperature correction factor of approximately −0.021 cm^{-1} K^{-1}, which is integrated into the conventional Raman shift–stress relationship to assess stress variations induced by temperature variations. The elastic modulus tensor of 4H-SiC at various temperatures determined using molecular dynamics simulations indicates a linear reduction in modulus with increasing temperature. This variable temperature modulus is incorporated into the Raman shift–stress relationship. Furthermore, a finite element method is used for model simplification to perform stress calculations in three axial directions. The experimental results confirm the consistency between calculated and experimental values with a 10% error range under the uniaxial stress condition. The study findings provide valuable insights into assessing stress evolution in 4H-SiC under temperature variations based on Raman spectroscopy, thereby advancing the application of spectroscopic techniques in material stress detection.

1. Introduction

SiC has emerged as a promising alternative for applications of power electronics owing to its remarkable physical properties, such as wide bandgap, low density, and high thermal conductivity. Among the multiple polytypes of SiC, the 4H polytype is particularly notable because of its higher critical electric-field strength, superior electrical mobility, and lower defect density than those of the 3C and 6H polytypes.[1–4] However, the inherent rigidity of 4H-SiC presents substantial challenges during manufacturing because it introduces strong mechanical stress. As this inferiority significantly restricts the application of 4H-SiC, there is an increased research interest to address this issue.[5–8] To date, most studies on the internal stress in 4H-SiC have employed non-destructive evaluation technologies, such as X-ray diffraction (XRD)[9,10] and the curvature method.[11] However, these methods offer only millimeter-scale spatial resolution,[12] which is inadequate for providing the necessary insights into micro-scale stress

Z. Yang, X. Wang, Z. Tang, B. Guo, H. Tang, R. Zhang, J. Fan
Shanghai Engineering Technology Research Center for SiC Power Device
Academy for Engineering & Technology
Fudan University
Shanghai 200433, China
E-mail: hongyu_tang@fudan.edu.cn; rjzhang@fudan.edu.cn; jiajie_fan@fudan.edu.cn

Y. Zuo, J. Zhang, J. Fan
Research Institute of Fudan University in Ningbo
Ningbo 315336, China

R. Zhang
School of Information Science and Technology
Fudan University
Shanghai 200433, China

X. Fan
Department of Mechanical Engineering
Lamar University
PO Box 10028, Beaumont, TX 77710, USA

G. Zhang, J. Fan
EEMCS Faculty
Delft University of Technology
Delft 2628, the Netherlands

The ORCID identification number(s) for the author(s) of this article can be found under https://doi.org/10.1002/lpor.202401033

DOI: 10.1002/lpor.202401033

distributions. Therefore, there exists a critical need for the development of innovative non-destructive techniques to detect microscale stresses in 4H-SiC.

Raman spectroscopy, which relies on the principle of inelastic scattering between photons and matter, is an invaluable non-destructive characterization tool that effectively captures material characteristics.[13] Sugiyama et al.[14] utilized four-point bending experiments to establish a quantitative relationship between the Raman shift and stress of 4H-SiC crystals. Their study significantly advanced 4H-SiC stress detection in a rapid, contactless, and non-destructive manner.[15] Furthermore, Yoshikawa et al.[16] employed Raman spectroscopy to investigate the visual stress distribution within a 4H-SiC metal–oxide–semiconductor field-effect transistor under various polarization states, revealing significant stress variations near critical device components. Izumi et al.[17] extended this approach to explore the 4H-SiC stress distribution beneath Al electrodes in power devices, laying the foundation for further in-depth research using finite element method (FEM) analyses.

Existing research on 4H-SiC stress based on Raman spectroscopy predominantly focuses on room-temperature conditions,[18] resulting in a significant gap in the understanding of stress evolution at high temperatures. The failure analysis results of actual 4H-SiC devices have underscored the criticality of the stress damage induced by high temperatures.[19–21] Temperature variations can alter the equilibrium positions of atoms, bond strengths, and vibrational states within materials, significantly impacting the Raman peak characteristics such as peak positions, full width at half maximum (FWHM), and intensities.[22,23] However, the theoretical principle of Raman stress detection relies on the peak shift relative to the unstressed state, rendering the temperature-induced influence a significant obstacle in accurately assessing the stress-induced peak shift. Despite the importance of temperature in Raman stress analyses,[24,25] decoupling the temperature- and stress-induced peak shifts in the Raman spectroscopy of 4H-SiC at different temperatures remains a significant challenge. Therefore, the thermal and mechanical properties of 4H-SiC must be comprehensively investigated. This requires advanced experimental techniques and computational tools to effectively separate and quantify the individual effects of temperature and stress, which can enable Raman spectroscopy to detect the evolution of high-temperature-induced stress in 4H-SiC. This approach is crucial for the non-destructive evaluation of stress states within 4H-SiC devices as it offers critical insights into their performance and reliability under operational conditions.

In this study, we developed a Raman shift–stress prediction model for 4H-SiC, which meticulously incorporates the temperature effect. The 4H-SiC substrates and epitaxial samples, fabricated via chemical vapor deposition (CVD), were subjected to in situ variable-temperature Raman spectroscopy, revealing consistent temperature correction factors across a temperature range of 30 to 530 °C. The Raman shift–stress relationship was established by integrating this factor into the prediction model, which facilitated precise detection of the microscopic stress distribution within 4H-SiC at varying temperatures. Furthermore, as the elastic modulus of material changes with temperature, we improved the conventional Raman shift–stress relationship by utilizing molecular dynamics (MD) simulations to compute the elastic modulus tensor of 4H-SiC at different temperatures. These values were pivotal for comprehensively understanding the stress responses of the material under diverse temperature conditions. Based on these elastic modulus values, the average in-plane axial stress components were determined via FEM, thereby simplifying the Raman shift–stress relationship. This study not only proposes an effective methodology for evaluating the stress behavior of 4H-SiC in high-temperature environments but also enriches the theoretical comprehension of its stress evolution under such conditions.

2. Results and Discussion

2.1. Characterization of Substrate and Epitaxial Layers

In the existing 4H-SiC power devices, the 4H-SiC chip typically includes a homogeneous epitaxial layer. Therefore, we selected 4H-SiC substrates and homogeneous epitaxial layers for our analysis. We aimed to identify the specific similarities and differences between the materials by comparing these two sample types to establish a foundation for Raman-based stress detection in future device applications. In this study, CVD was used to uniformly fabricate an epitaxial layer on a 4H-SiC substrate. Considering the influence of stress accumulation on the microstructure during epitaxial growth, a buffer layer technology was implemented as a mitigation strategy. Two epitaxial samples were prepared for comparative analysis: one with a buffer layer (referred to as EPI-B) and the other without a buffer layer (referred to as EPI). The results of the XRD analysis (Figure S1, Supporting Information) confirm that the crystalline phase of the epitaxial layer is consistent with that of the substrate, which can be well indexed to 4H-SiC (point group: 6mm; space group: $P6_3mc$).[26,27] Notably, the absence of peaks other than the pronounced (0004) peak of 4H-SiC within the scope of this measurement revealed that the epitaxial growth was directed along the crystal plane of the substrate. Moreover, the sharpness of the XRD peak indicated the high purity and crystallinity of the homoepitaxial layer.

Initial assessments of the surface morphology, conducted via optical microscopy, aimed to investigate the macroscopic surface features of both pre- and post-epitaxial growth samples. This comparison between the epitaxial layers and the original substrate (referred to as SUB) revealed that the epitaxial layers maintained surface flatness post-growth, indicating that the epitaxial process had no detrimental effects on the surface morphology (Figure S2, Supporting Information). Detailed observations were performed at a microscopic level using scanning electron microscopy (SEM). High-resolution SEM images (**Figure** 1a,e,i) revealed that both the EPI-B and EPI samples exhibited remarkable smoothness and uniformity, demonstrating the effectiveness of the CVD process in maintaining the consistency of the epitaxial layers regardless of the presence of the buffer layer. SEM cross-sectional analysis measured the thickness of the epitaxial layers (Figures S3–S5, Supporting Information), indicating an increase in thickness from approximately 362 μm (SUB) to 372 μm post-epitaxy (Figure S6, Supporting Information). Additionally, the SEM cross-sectional analysis demonstrated the flatness of the epitaxial surface, corroborating the uniform thickness of the epitaxial layer (Figure 1b,f,j).

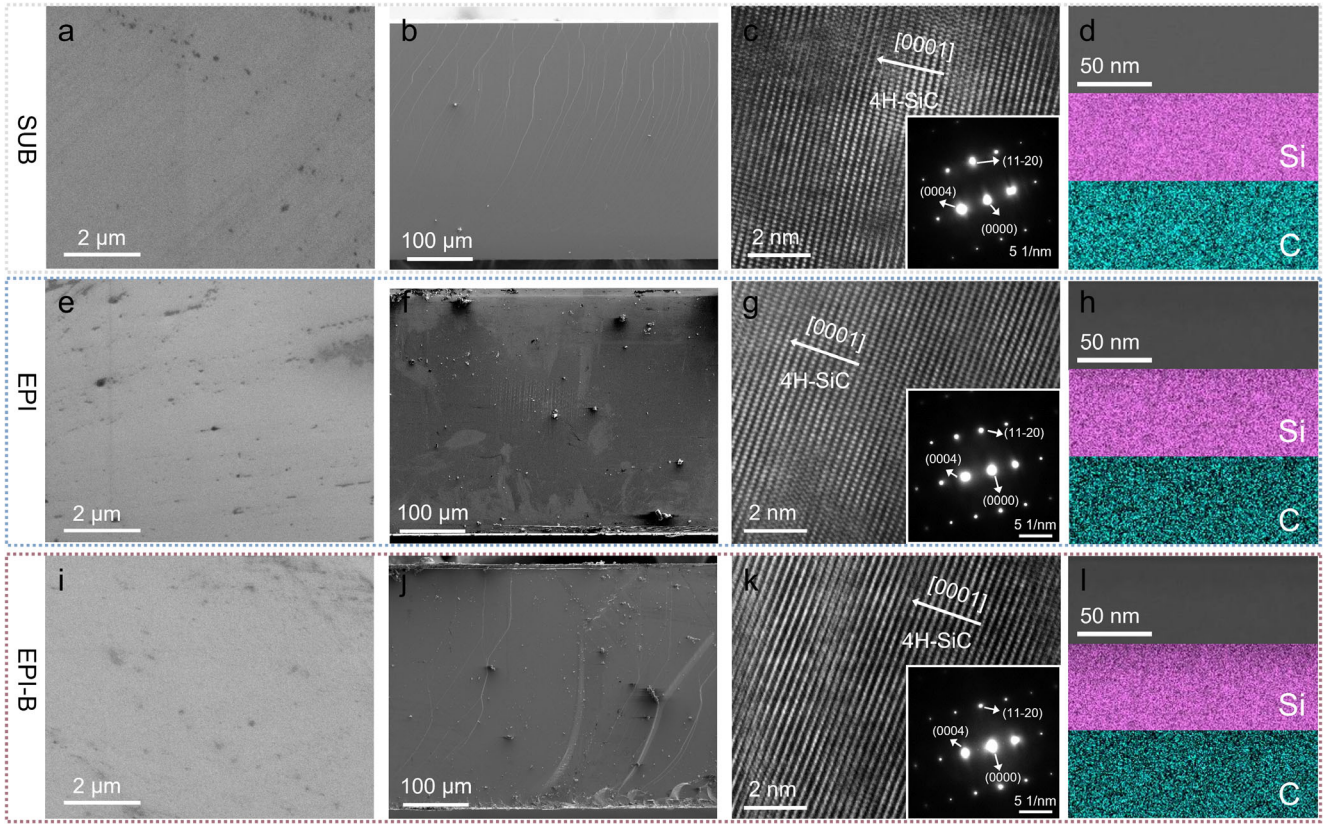

Figure 1. Basic structural characterization of samples. Scanning electron microscopy (SEM) surface morphology of the a) substrate, e) epitaxial layer without the buffer layer, and i) epitaxial layer with the buffer layer. SEM cross-sectional morphology of the b) substrate, f) epitaxial layer without the buffer layer, and j) epitaxial layer with the buffer layer. High-resolution transmission electron microscopy (HRTEM) images of the c) substrate, g) epitaxial layer without the buffer layer, and k) epitaxial layer with the buffer layer. The corresponding energy-dispersive X-ray spectroscopy (EDX) elemental mapping of Si and C in transmission electron microscopy (TEM) mode for the d) substrate, h) epitaxial layer without the buffer layer, and l) epitaxial layer with the buffer layer in the TEM samples.

To elucidate the uniformity of the crystal structure and ascertain the directional growth of the EPI-B and EPI samples on a microscopic scale, the samples were prepared using focused ion beam (FIB) technology for high-resolution transmission electron microscopy (HRTEM) analysis. Figure 1c,g,k indicate that both the epitaxial layer and substrate have a 4H-SiC crystal structure and exhibit identical growth orientations along the (0001) crystal plane.[28,29] The longitudinal HRTEM results in Figures S7 and S8 (Supporting Information) further demonstrate the excellent consistency between the epitaxial layer and the substrate structure. Additionally, energy-dispersive X-ray spectroscopy (EDX) composition analysis performed based on TEM demonstrated a uniform distribution of Si and C within the epitaxial layer (Figure 1d,h,l), indicating a uniform material composition throughout the growth process.

X-ray photoelectron spectroscopy (XPS) was utilized to precisely analyze the chemical composition of the samples. Full-spectrum scans indicated consistent energy spectra across all the samples, with prominent Si and C signals (Figure S9, Supporting Information). **Figure** 2a,b illustrates high-resolution XPS scans of the 4H-SiC sample. In the Si 2p spectrum (Figure 2a), two primary peaks can be distinctly discerned at 100.4 eV (Si $2p_{3/2}$) and 101.1 eV (Si $2p_{1/2}$), precisely aligning with the standard Si 2p spectrum of 4H-SiC.[30,31] In the high-resolution C 1*s* spectrum (Figure 2b), the strong peak centered at 282.5 eV can be attributed to the Si—C bond inherent to 4H-SiC.[30,31] Additionally, a weak broad peak is observed at 283.8 eV, suggesting the presence of additional bonded states such as C—C, Si—C—O, and C—O configurations.[31]

Room-temperature Raman spectroscopy was conducted on both the epitaxial samples and the substrate to assess the impact of epitaxial growth on internal stress. Figure 2c indicates that the epitaxial growth process introduces tensile stress in the crystal lattice, as evidenced by the redshift of the E_2(TO) Raman peak. In particular, the E_2(TO) peak of the substrate and the EPI-B sample are positioned at approximately 777 cm^{-1}, corresponding to a relatively stress-free state at room temperature (30 °C).[17,32] By contrast, the EPI sample exhibits a notable redshift, highlighting the significant role of the buffer layer in mitigating stress accumulation during the epitaxial growth process.

Additionally, a broad peak near the A_1(LO) vibrational peak in the epitaxial sample confirmed the presence of the plasmon–phonon coupling effect.[33] This phenomenon is particularly evident in polar semiconductor materials, such as 4H-SiC. This effect, facilitated by the interaction of free carriers in

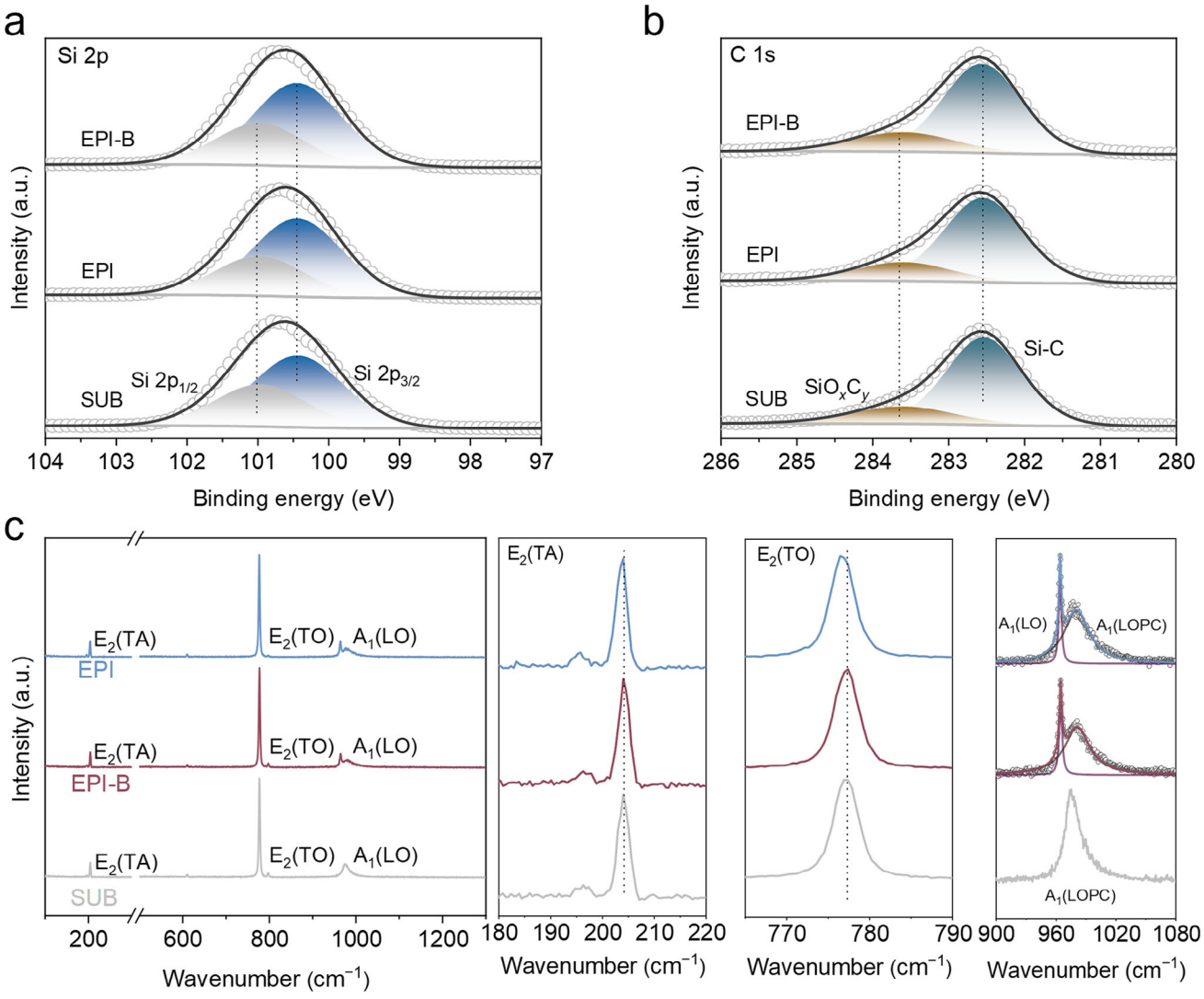

Figure 2. Composition analysis of epitaxial samples. X-ray photoelectron spectroscopy (XPS) characterization of a) Si 2p spectrum and b) C 1s spectrum. c) Raman spectrum at room temperature (30 °C).

the N-doped 4H-SiC substrate with lattice phonons upon photoexcitation,[22,32] exhibited the longitudinal optical phonon coupling mode near 980 cm^{-1}.[34,35] By contrast, the epitaxial samples exhibited an additional A_1(LO) peak, a characteristic of the intrinsic nature of undoped crystals. Meticulous peak fitting analysis of the Raman spectra enabled the determination of the A_1(LO) peak within the epitaxial layer, identifying its position at approximately 964 cm^{-1}.[32]

2.2. Variable-Temperature Phonon Behavior of 4H-SiC

The primary objective of the study is to comprehensively analyze the Raman frequency shifts in three 4H-SiC samples, namely, SUB, EPI, and EPI-B, over a wide temperature range of 30–530 °C. We used the in situ variable-temperature Raman spectroscopy to explore the phonon behavior in response to temperature variations in these materials.

As the temperature increased, the Raman peak positions of all samples consistently shifted towards longer wavelengths (redshift), as shown in Figure S10 (Supporting Information) and **Figure 3**. Notably, the E_2(TO) and A_1(LO) modes exhibited more significant redshifts than the E_2(TA) mode. This difference in the magnitude of the redshift between the acoustic and optical vibrational modes highlighted their distinct response mechanisms to temperature variations.[36] As the temperature increased, the acoustic vibration modes such as E_2(TA) predominantly responded to the reduction in the restoring force induced by the intensification of the lattice vibration, resulting in a redshift. This shift indicated the increasing lattice vibration energy and its impact on the lattice parameters as the temperature increased. By contrast, the redshift in the optical modes (E_2(TO) and A_1(LO)) originated from the increased relative atomic motion with the increasing temperature, which weakened the atomic interactions within the crystal lattice and unit cell. Owing to their unique mechanisms of relative motion within the crystal, the

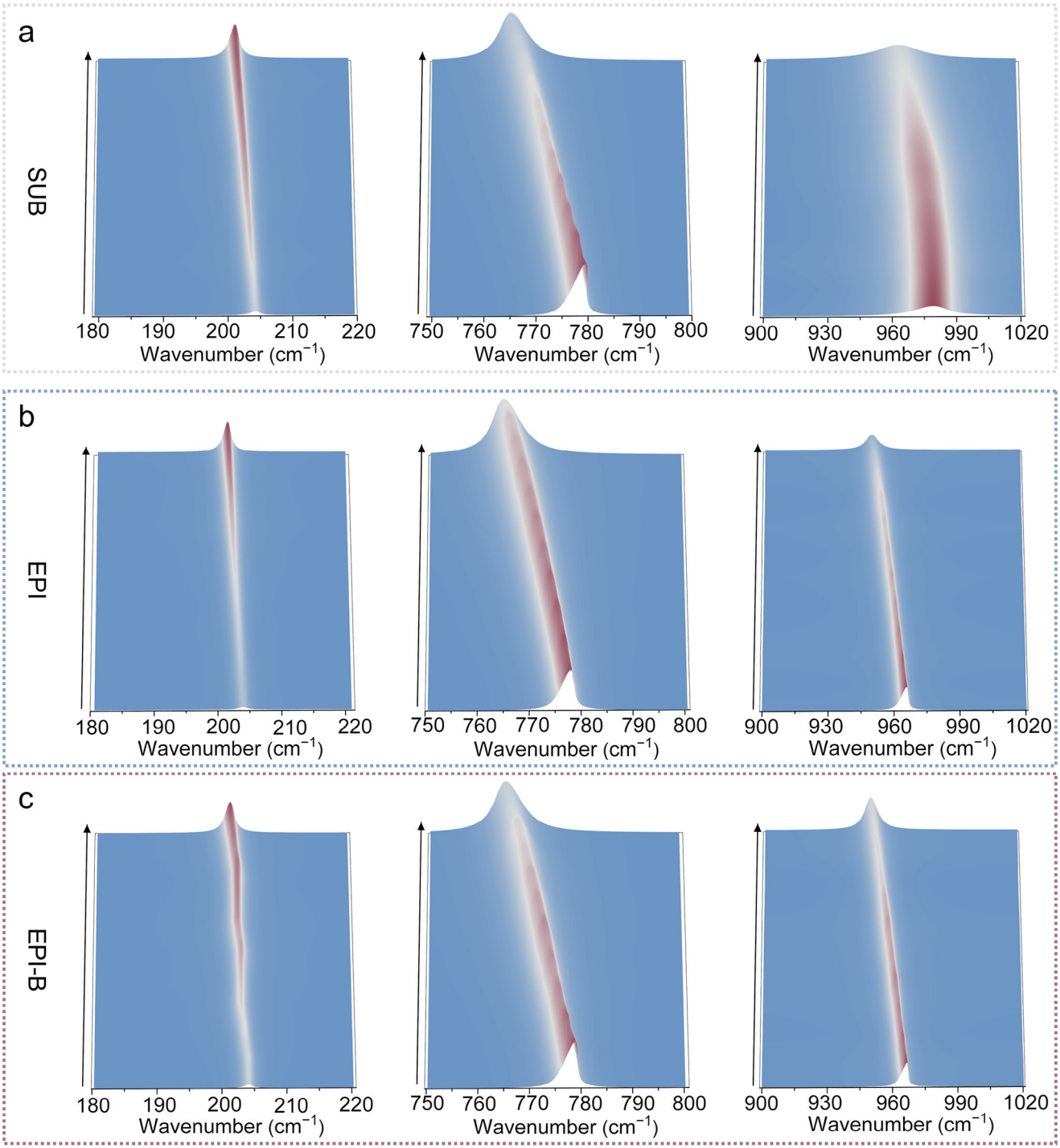

Figure 3. In situ Raman spectrum measurement with the temperature ranging from 30 °C to 530 °C and the main intensity peak versus temperature. a) Substrate, b) epitaxial layer without the buffer layer, and c) epitaxial layer with the buffer layer.

intrinsic differences in the lattice dynamic behaviors between these vibrational modes further contributed to their varying redshift amplitudes.

The effect of temperature on the intensity of Raman peaks exhibited different tendencies. With the increasing temperature, the intensities of the E_2(TO) and A_1(LO) peaks decreased significantly, whereas that of the E_2(TA) peak tended to increase. This increase in intensity can be attributed to the enhanced phonon mode activity and its positive correlation with phonon scattering probability.[37,38] As the temperature increases, the increase in the average number of phonons improves the probability of phonon scattering, which in turn enhances the intensity of Raman peaks.

We conducted detailed variable-temperature fittings of the peak positions for the E_2(TA), E_2(TO), and A_1(LO) modes to

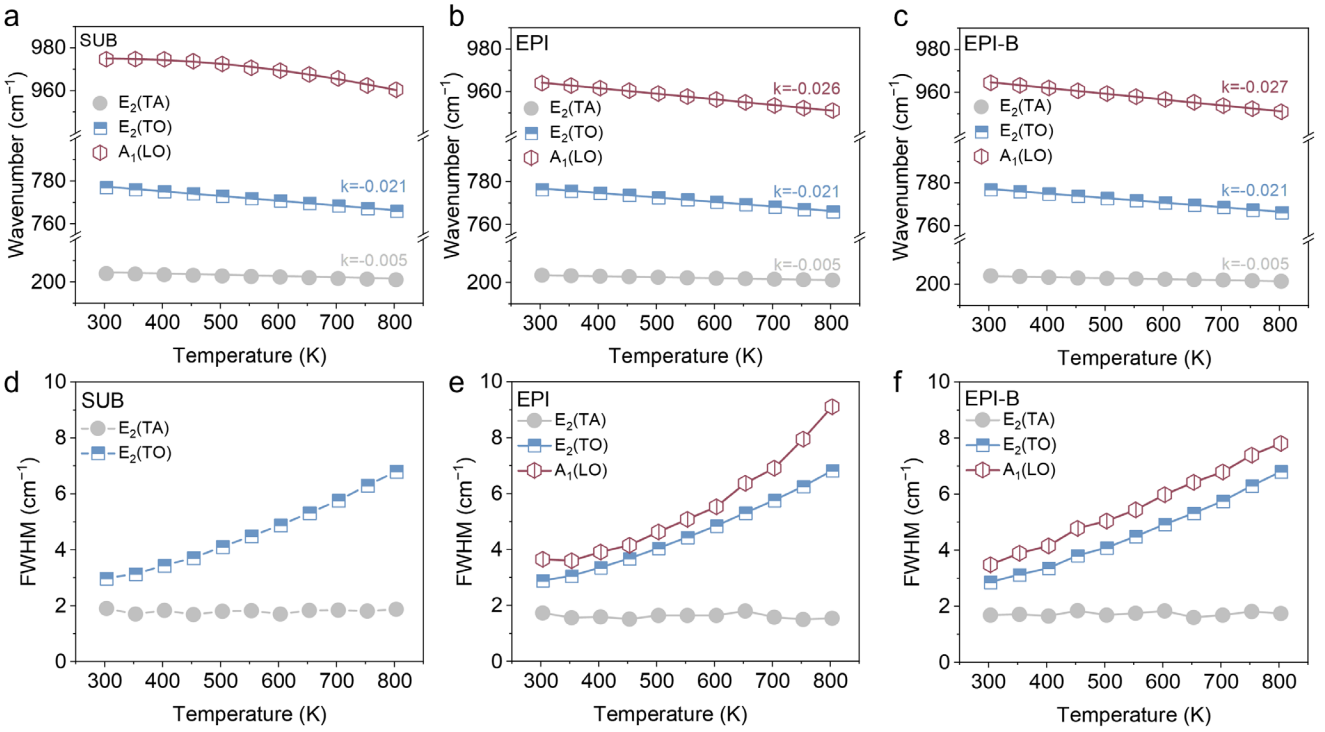

Figure 4. Position of the peak and full width at half maximum (FWHM) of the main peak versus temperature. Relationship among the a) substrate, b) epitaxial layer without the buffer layer, and c) epitaxial layer with the buffer layer between the peak position and temperature, where *k* represents the slope. The linewidth versus temperature is depicted for the d) substrate, e) epitaxial layer without the buffer layer, and f) epitaxial layer with the buffer layer.

accurately characterize the Raman frequency shifts of the three samples at varying temperatures. The fitting results for E_2(TA) and E_2(TO) revealed a linear relationship between the peak positions and temperature (**Figure** 4a–c). A comparative analysis verified the consistency between the temperature coefficients of E_2(TA) (approximately -0.005 cm^{-1} K^{-1}) and E_2(TO) (approximately -0.021 cm^{-1} K^{-1}) across all samples, indicating no significant variation in thermal expansion properties between the epitaxial layers and the substrate of 4H-SiC. This consistency implied that the epitaxial layers maintained the same crystal quality as the substrate (Figure 4a).

In comparison with the Raman peak shift, the variations in the FWHM with temperature were primarily attributed to the anharmonic attenuation and scattering of phonons. Analysis of the FWHM alterations for the E_2(TO) and A_1(LO) modes at elevated temperatures indicated significant broadening, implying an increase in the number of phonons and scattering probabilities, which reduced the average phonon lifetimes. The broadening was more pronounced in the A_1(LO) mode (>4 cm^{-1}) than that in the E_2(TO) mode (<4 cm^{-1}), as shown in Figure 4e,f; this can be attributed to additional phonon attenuation pathways in the A_1(LO) mode. Furthermore, the acoustic mode E_2(TA) exhibited no significant broadening (Figure 4d–f).

Defects within the material significantly affect the phonon scattering process, thereby influencing the phonon lifetime.[39–41] To investigate the crystal quality of the epitaxial samples further, we focused on the phonon lifetime in the E_2(TO) mode as a critical parameter for assessment because this mode exhibited the strongest Raman peak. Initially, the variation in FWHM (Γ) in the E_2(TO) mode was fit with temperature using the four-phonon decay model, as follows:[23,42]

$$\Gamma(T) = A \times \left[1 + \sum_{i=1}^{2} n(T, \omega_i)\right] + B \times \left\{1 + \sum_{j=1}^{3} \left[n(T, \omega_j) + n^2(T, \omega_j)\right]\right\} \quad (1)$$

where the first term denotes the three-phonon interaction process, delineated as $\omega_1 + \omega_2 = \omega_0$; and the second term corresponds to the four-phonon interaction process, expressed as $\omega_1 + \omega_2 + \omega_3 = \omega_0$. The three- and four-phonon interaction processes were assumed to be symmetrical to simplify the calculations. Accordingly, $\omega_1 = \omega_2 = 1/2\omega_0$ and $\omega_1 = \omega_2 = \omega_3 = 1/3\omega_0$ for the three- and four-phonon interactions, respectively. Constants A and B indicate the fitting parameters linked to the three- and four-phonon decay processes, respectively. The terms $n(T,\omega_i)$ and $n(T,\omega_j)$ denote Bose–Einstein distribution functions, whereas ω_i and ω_j indicate the phonon frequencies corresponding to the three- and four-phonon processes, respectively.

The model predictions align well with experimental data, demonstrating the observed nonlinear broadening over the tested temperature range (**Figure** 5a–c). Subsequently, the phonon lifetime τ was calculated using the energy-time uncertainty principle, as follows:[42,43]

$$\frac{2\pi\Gamma(T)}{h} = \frac{1}{\tau} \quad (2)$$

where $h = 3.3284 \times 10^{-11}$ cm^{-1} s denotes the Planck constant.

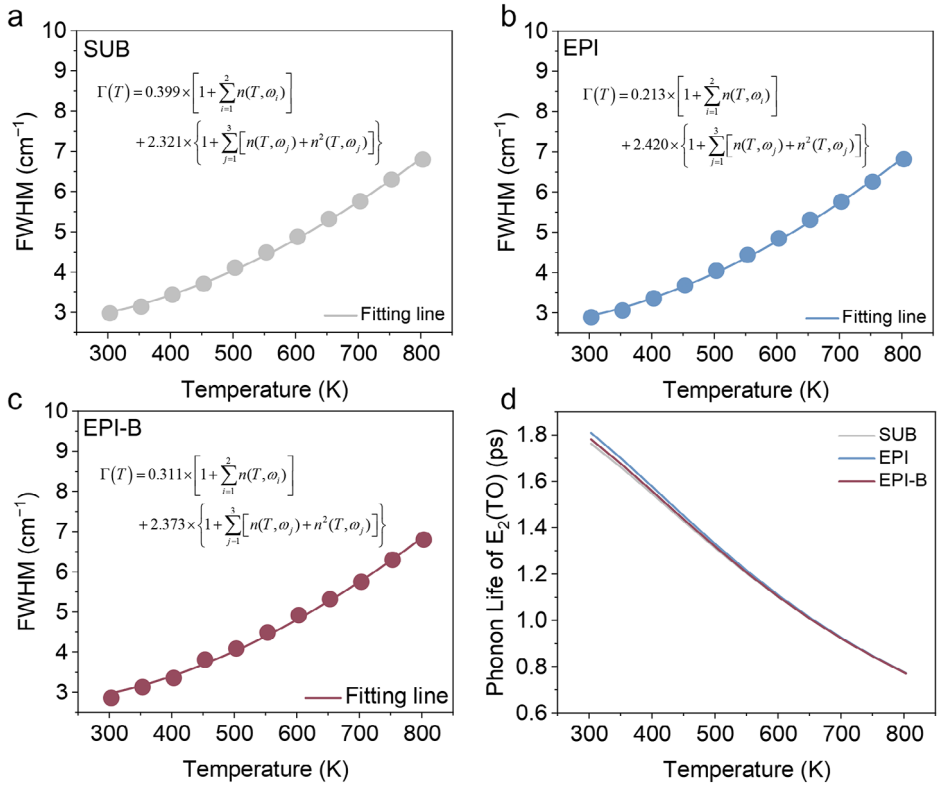

Figure 5. Fitting of the full width at half maximum (FWHM), temperature evolution of the E_2(TO) Raman peak, and the relationship between phonon lifetime and temperature. E_2(TO) linewidth fitting results of the a) substrate, b) epitaxial layer without the buffer layer, and c) epitaxial layer with the buffer layer. d) The E_2(TO) phonon lifetime of the sample changes with the temperature.

The results indicate a decrease in the phonon lifetime with increasing temperature, which is consistent with the expected increase in lattice vibrations at higher temperatures (Figure 5d). No significant differences were observed among the three samples, suggesting that the homoepitaxial 4H-SiC samples retained the high crystal quality of the original substrate.

The aforementioned analysis reveals the similarity in Raman spectral evolution between the epitaxial samples and the substrate across various temperatures, providing a robust experimental foundation for developing predictive relationships among temperature, stress, and Raman shift for 4H-SiC materials.

2.3. Raman Shift–Stress Relationship of 4H-SiC

Amilusik et al.[44] provided valuable insights into the phononic response of hexagonal material under stress conditions. Their findings revealed that the E_1(TO) and E_2(TO) vibrational modes are sensitive to stress variations, whereas the E_2(TA) and A_1(LO) modes are insensitive to axial stress variations. Consequently, the E_2(TO) mode is extensively used as a base for developing a predictive relationship that correlates the Raman shift at different temperatures with the stress in 4H-SiC.

2.3.1. Stress Prediction Model of 4H-SiC

The crystal structure of 4H-SiC, which is a hexagonal system, comprises densely packed Si and C atoms. The experimental coordinate system is aligned with the crystallographic axes (**Figure 6**), with the [1−100], [11−20], and [0001] directions corresponding to the X-, Y-, and Z-axis, respectively. The E_2(TO) mode Raman tensor with C_{6V} symmetry exhibits double degeneracy.[45]

$$R^1_{E_2}=\begin{pmatrix}0 & d & 0\\ d & 0 & 0\\ 0 & 0 & 0\end{pmatrix},\quad R^2_{E_2}=\begin{pmatrix}d & 0 & 0\\ 0 & -d & 0\\ 0 & 0 & 0\end{pmatrix} \tag{3}$$

Under identical conditions of stretching direction and instrument polarization, the theoretical Raman shift–stress relationship for uniaxial stress closely matched the results of the relationship between uniaxial stress and Raman shift of 4H-SiC obtained using a four-point bending experiment ($\Delta\omega_{E2}=-1.96$ (cm^{-1} GPa^{-1}) $\times\,\Delta\sigma$ (GPa)).[14] The detailed derivation process is outlined in the second section of the Supporting Information. In the biaxial stress mode, the calculated result was compared with the test result ($\Delta\omega_{E2}=-3.1$ (cm^{-1} GPa^{-1}) $\times\,\Delta\sigma$ (GPa)).[25] The error between the calculated results and previously reported experimental data consistently remained within 10%.

Subsequently, based on the specific relationship between the room-temperature Raman shift and stress, the dual effects of stress and temperature on material deformation were considered. We combined Hooke's law with the interaction between mechanical stress–strain and thermal expansion deformation to accurately describe the crystal behavior in complex environments.

$$\varepsilon=S\Delta\sigma+\alpha\Delta T \tag{4}$$

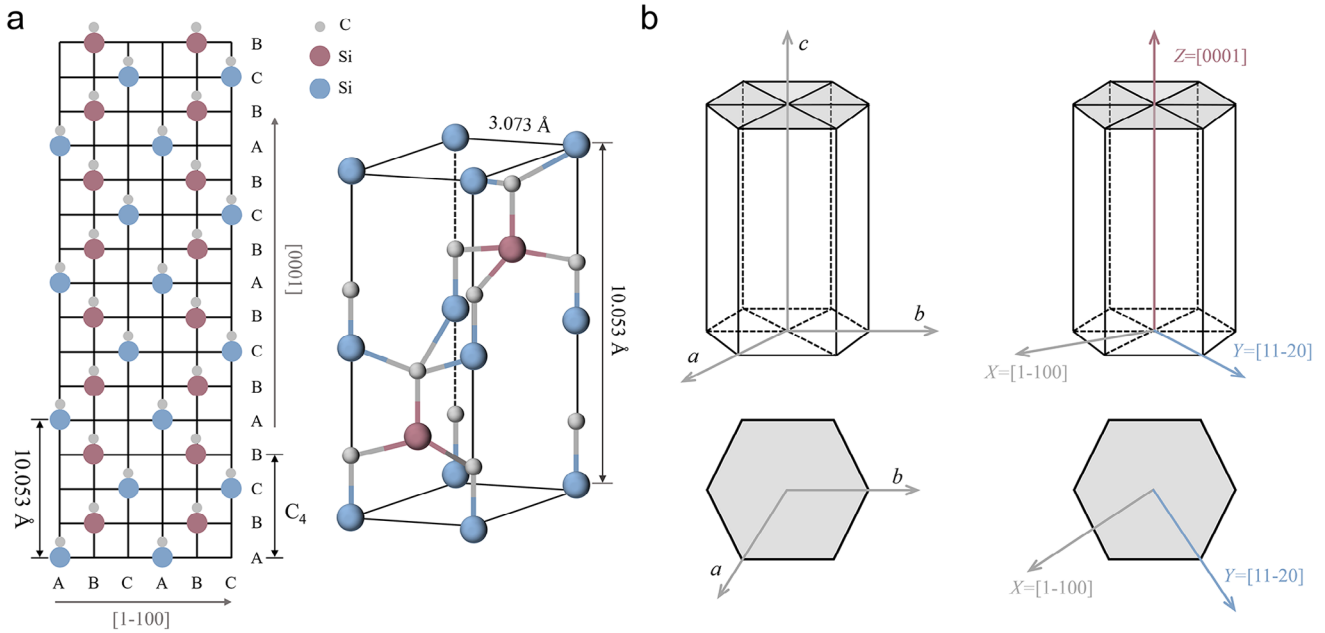

Figure 6. Schematic of the crystal structure and crystal coordinate system of 4H-SiC. a) Atomic arrangement and unit cell parameters of 4H-SiC. b) Construction of the crystal coordinate system.

where α represents the coefficient of thermal expansion; we set 303.15 K as the initial room temperature.

When temperature and stress coexist, the constitutive relationship for deformation can be determined based on crystal symmetry, as follows:

$$\begin{pmatrix} \epsilon_{xx} \\ \epsilon_{yy} \\ \epsilon_{zz} \\ 2\epsilon_{yz} \\ 2\epsilon_{zx} \\ 2\epsilon_{xy} \end{pmatrix} = \begin{pmatrix} s_{11} & s_{12} & s_{13} & & & \\ s_{12} & s_{11} & s_{13} & & & \\ s_{13} & s_{13} & s_{33} & & & \\ & & & s_{44} & & \\ & & & & s_{44} & \\ & & & & & 2\left(s_{11}-s_{12}\right) \end{pmatrix} \begin{pmatrix} \Delta\sigma_{xx} \\ \Delta\sigma_{yy} \\ \Delta\sigma_{zz} \\ \Delta\sigma_{yz} \\ \Delta\sigma_{zx} \\ \Delta\sigma_{xy} \end{pmatrix} + \alpha\Delta T \tag{5}$$

By substituting Equation 5 in Equation S11 (Supporting Information), the functional relationship describing the frequency change in the E_2(TO) mode caused by the stress and temperature fluctuations can be expressed as follows:

$$\begin{aligned} \Delta\omega_{E_2} = & \left[a_{E_2}\left(s_{11}+s_{12}\right)+b_{E_2}s_{13}\right]\left(\Delta\sigma_{xx}+\Delta\sigma_{yy}\right) \\ & +\left(2a_{E_2}s_{13}+b_{E_2}s_{33}\right)\Delta\sigma_{zz} \\ & \pm c_{E_2}\left|s_{11}-s_{12}\right|\sqrt{\left(\Delta\sigma_{xx}-\Delta\sigma_{yy}\right)^2+4\Delta\sigma_{xy}^2}+\chi\Delta T \end{aligned} \tag{6}$$

where χ denotes the temperature-induced frequency shift coefficient, measured to be approximately -0.021 cm^{-1} K^{-1} in in situ variable-temperature Raman experiments.

Studies have reported that the mechanical properties of materials tend to soften with an increase in temperature.[46,47] This phenomenon is critical for understanding the material behavior under high-temperature conditions. However, existing studies primarily focus on calculating the elastic constant tensor based on first-principles methods, without considering the effect of temperature on material properties.[48,49] This omission can compromise the accuracy of the models when predicting the behavior of materials under high-temperature-induced stress. To address this gap, we employed MD simulations to calculate and analyze the values of the elastic constant tensor for 4H-SiC crystals across a spectrum of temperatures (**Figure 7**). The specific procedures for calculating the elastic modulus and compliance coefficient tensors are outlined in the Supporting Information. Table S1 (Supporting Information) summarizes the data obtained from the simulations, which are consistent with the results reported in the existing literature.[50,51] Figure 7a,b illustrates the temperature-dependent changes in these tensors, where the elastic constants decrease and the compliance coefficient tensors increase with the increase in temperature (except for the s_{12} and s_{13} components).

By modifying the compliance coefficient relationship in Equation 6, the predicted relationship between the temperature, Raman shift, and stress can be obtained under the action of triaxial stress.

$$\begin{aligned} \Delta\omega_{E_2} = & \left[a_{E_2}\left(s_{11,\mathrm{RT}}+s_{12,\mathrm{RT}}\right)+b_{E_2}s_{13,\mathrm{RT}}\right. \\ & \left.+\left(a_{E_2}k_{11}+a_{E_2}k_{12}+b_{E_2}k_{13}\right)\Delta T\right]\left(\Delta\sigma_{xx}+\Delta\sigma_{yy}\right) \\ & +\left[\left(2a_{E_2}s_{13,\mathrm{RT}}+b_{E_2}s_{33,\mathrm{RT}}\right)+\left(2a_{E_2}k_{13}+b_{E_2}k_{33}\right)\Delta T\right]\Delta\sigma_{zz} \\ & \pm c_{E_2}\left|\left(s_{11,\mathrm{RT}}-s_{12,\mathrm{RT}}\right)+\left(k_{11}-k_{12}\right)\Delta T\right| \\ & \times\sqrt{\left(\Delta\sigma_{xx}-\Delta\sigma_{yy}\right)^2+4\Delta\sigma_{xy}^2}+\chi\Delta T \end{aligned} \tag{7}$$

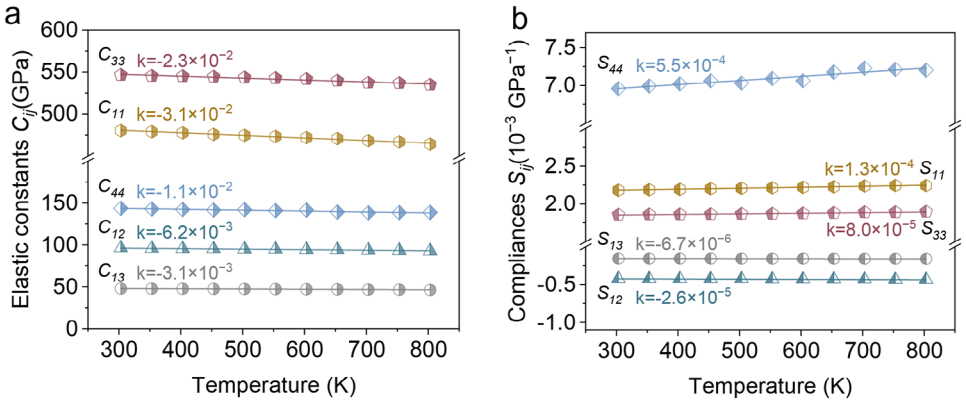

Figure 7. Calculated temperature dependence of the elastic modulus and compliance coefficient of 4H-SiC. a) Elastic modulus versus temperature. b) Compliance coefficient versus temperature. The values of *k* in (ab) denote the slope.

where RT represents the temperature corresponding to 303.15 K. The analysis reveals that in the temperature range of 303.15–803.15 K, the variation in the compliance coefficient owing to the temperature change is significantly smaller than the values of other terms. Consequently, this term can be neglected, simplifying the formula as:

$$\Delta\omega_{E_2} = \left[a_{E_2}(s_{11,\mathrm{RT}} + s_{12,\mathrm{RT}}) + b_{E_2} s_{13,\mathrm{RT}}\right](\Delta\sigma_{xx} + \Delta\sigma_{yy}) + \left(2a_{E_2} s_{13,\mathrm{RT}} + b_{E_2} s_{33,\mathrm{RT}}\right)\Delta\sigma_{zz} \pm c_{E_2}\left|s_{11,\mathrm{RT}} - s_{12,\mathrm{RT}}\right| \times \sqrt{(\Delta\sigma_{xx} - \Delta\sigma_{yy})^2 + 4\Delta\sigma_{xy}^2} + \chi\Delta T \quad (8)$$

2.3.2. Finite Element Simulation Analysis

We performed a series of FEM simulations to quantify the relationship between the axial-stress components and their adaptation to temperature fluctuations (Figures S14–S17, Supporting Information). These simulations provide a detailed analysis of stress accumulation on the material surface over a temperature range of 30–530 °C. The results indicated that the stress was predominantly concentrated in the central region, with a relatively uniform distribution. Further analysis was used to calculate the average magnitude of each stress component at various temperatures (Figure S18, Supporting Information), indicating comparable stress values along the X-axis and Y-axis (Tables S2–S5, Supporting Information).

Additionally, the axial stress along the Z-axis and shear stress in the XY plane were significantly lower than the axial stresses along the X-axis and Y-axis, simplifying the in-plane residual stress into a biaxial model ($\Delta\sigma_{xx} = \Delta\sigma_{yy} \neq 0$, $\Delta\sigma_{zz} = 0$); the shear stress in the XY plane was also negligible ($\Delta\sigma_{xy} = 0$). This simplification enabled the derivation of the specific Raman shift–stress relationship for the in-plane equibiaxial stress state, as follows:

$$\Delta\omega_{\mathrm{obs}} = -3.33\ (\mathrm{cm^{-1}\ GPa^{-1}}) \times \Delta\sigma\ (\mathrm{GPa}) - 0.021\ (\mathrm{cm^{-1}\ K^{-1}}) \times \Delta T\ (\mathrm{K}) \quad (9)$$

The derived simplified model captures the complex interactions between temperature and stress in terms of the deformation behavior of hexagonal crystalline materials, such as 4H-SiC, thereby providing a robust theoretical basis for an in-depth understanding of material behavior under high-temperature conditions.

2.4. Experiment Verification

We performed an in situ uniaxial tensile test on 4H-SiC crystal with a (0001) crystal plane at 250 °C to validate the calculation results of the theoretical model. Initially, Raman spectroscopy was performed at each tensile load (**Figure** 8a). We observed that the E_2(TO) peak redshifted as the tensile stress increased (Figure 8b). Subsequently, the tensile stress and Raman shift values of the E_2 peak were plotted as the X- and Y-axis parameters, respectively, to construct a coordinate diagram of the experimental data (Figure 8c). The solid line in the figure represents the linear fitting slope corresponding to the experimental data and the Raman shift–stress coefficient calculated using the least-squares method. According to the fitting results, the Raman shift–stress relationship of the 4H-SiC crystal on the (0001) crystal plane under uniaxial stress at 250 °C is $\Delta\omega = -1.98$ (cm^{-1} GPa^{-1}) × $\Delta\sigma$ (GPa)−4.58 (cm^{-1}). According to Equation 6, the theoretical result of the 4H-SiC crystal on the (0001) crystal plane is $\Delta\omega = -2.08$ (cm^{-1} GPa^{-1}) × $\Delta\sigma$ (GPa)−4.62 (cm^{-1}). This comparison revealed that the relative error between the experimental and theoretical results was less than 10%, establishing a foundation for the practical application of the predictive relationship.

3. Conclusion

In this study, we developed a 4H-SiC Raman shift–stress prediction model under the influence of temperature. We subjected the 4H-SiC samples to rigorous in situ variable-temperature Raman experiments, demonstrating that the Raman peaks remained consistently related to temperature fluctuations. A comparative analysis of the substrates and epitaxial samples revealed that the homoepitaxial process exhibited a minimal impact on this

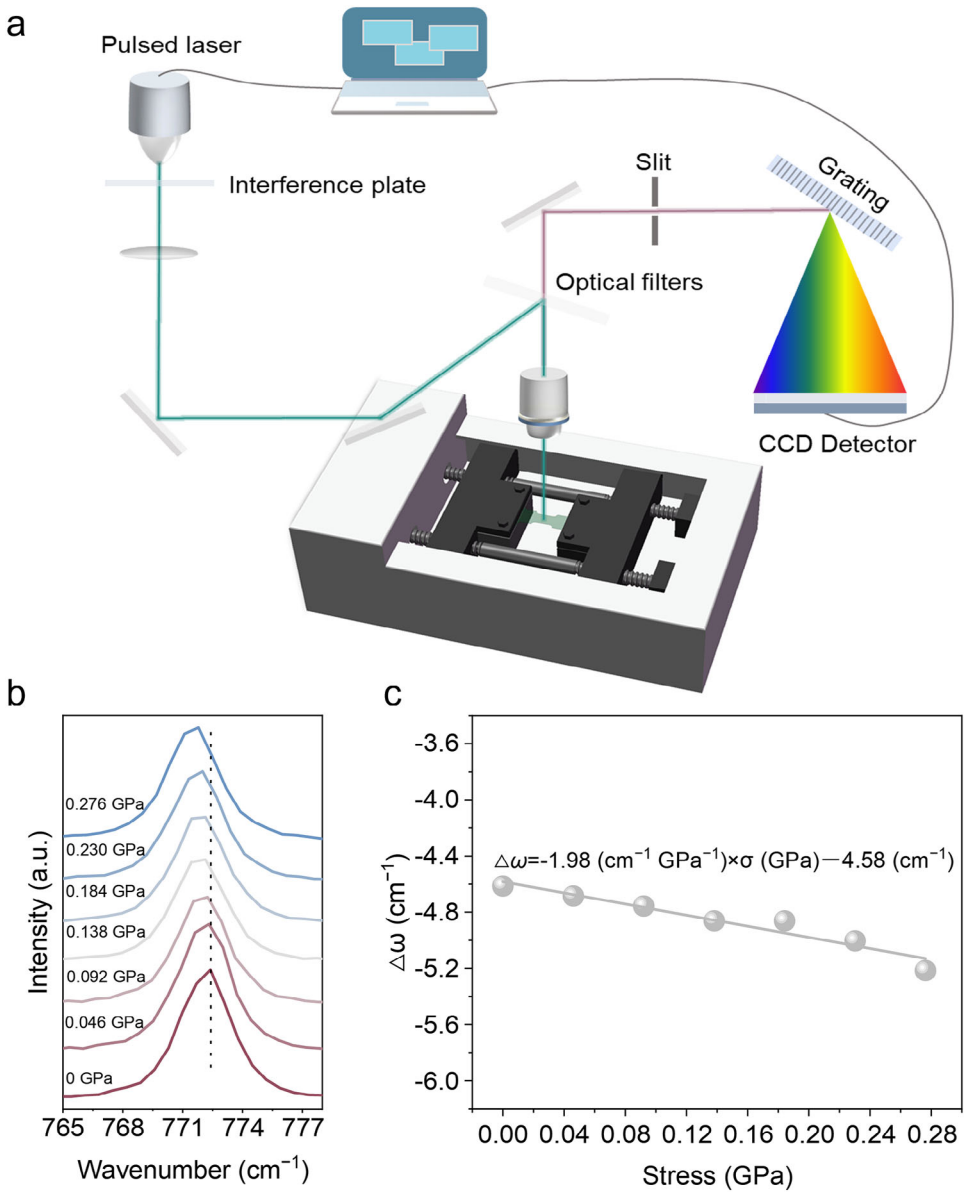

Figure 8. Experimental verification test. a) Schematic of the test device. b) Raman peak shift of the E_2(TO) mode under different tensile loads. c) Fitting relationship between the tensile load and Raman peak shift.

relationship. This finding provides a robust foundation for developing a universal predictive relationship that integrates temperature, stress, and Raman peak shifts. Furthermore, we derived a temperature correction factor to enhance the accuracy of the model by counteracting the errors induced by temperature variations. This relationship was further refined by integrating data from MD simulations, which provided temperature variations in the elastic modulus tensor of 4H-SiC. We used FEM to calculate the average axial stress across the sample plane, thereby simplifying the predictive model. The experimental verification results confirmed that the experimental and calculated values concur within an error range of 10% under a uniaxial stress state. The study findings can advance the understanding of stress detection in 4H-SiC in high-temperature environments, paving the way for non-contact and non-destructive temperature monitoring in real-time conditions.

4. Experimental Section

Homoepitaxial Preparation of 4H-SiC: A 4H-SiC homoepitaxial layer was deposited in a horizontal hot-wall CVD reactor. During the experiment, 4H-SiC served as the substrate for the epitaxial film. The growth environment within the reactor comprised a gaseous mixture of silicon tetrachloride ($SiHCl_3$), ethylene (C_2H_4), and hydrogen (H_2). $SiHCl_3$ and C_2H_4 were employed as the Si and C sources, respectively, to facilitate the homoepitaxial growth of 4H-SiC on the substrate. H_2 was primarily employed as the diluent, carrier, and etching gas. The growth temperature and chamber pressure were maintained at 1570 °C and 40 Torr, respectively, adhering

to standard process conditions. The C/Si ratio was precisely controlled at 1.0, and the epitaxial growth duration was set at 30 min. Additionally, the buffer layer was grown prior to the standard epitaxial growth. Further experimental details on the homoepitaxial growth of 4H-SiC are reported in a previous study.[52]

Material Characterizations: The surface morphology of the homoepitaxial sample was examined using optical microscopy. The crystal structure was characterized via XRD (Bruker, Germany), under Cu Kα radiation (λ = 1.5406 Å) with a scan range of 20°–80°. SEM was used to observe the microscale surface and cross-sectional morphologies using Zeiss GeminiSEM 360 (Germany). The TEM samples were prepared via FIB milling using the Zeiss Crossbeam 550 (Germany) and Thermo Fischer Helis 5 CX (USA). TEM analysis was performed using JEM-F200 (Japan) at an acceleration voltage of 200 kV, enabling the acquisition of selected area electron diffraction patterns and EDX spectra. XPS measurements were obtained using the Thermo Fischer ESCALAB 250Xi (USA), employing a monochromatic Al source ($h\nu$ = 1486.6 eV) under ultra-high vacuum conditions (8 × 10^{-10} Pa). Raman spectroscopy was performed using the micro-Raman spectrometer (HORIBA, Japan), which was initially calibrated with a single crystal silicon peak at 520.7 cm^{-1}. The light was collected using a 100x long working distance lens, with a grating density of 1800 gr mm^{-1} and a 532 nm helium–neon laser. The laser power was adjusted to approximately 5% of the total intensity. The experiments were conducted with a backscattering configuration using non-polarized detection. The sample was subjected to in situ heating via an electric stage, with temperature variations ranging from 30 °C to 530 °C; the heating interval was 50 °C. Each temperature point was maintained for 5 min before Raman spectroscopy to ensure uniform internal temperature within the sample. The sample was refocused after each temperature adjustment, and the Raman spectrum was collected after stabilizing the temperature to accurately capture the thermal effects on the vibrational properties of the sample. Uniaxial tensile tests were performed on the 4H-SiC sample using a micro in situ variable-temperature tensile tester (MICROTEST 300, Gatan Inc., USA). The sample size was set according to fixture standards. Tensile tests were performed at intervals of 25 N and finally loaded to 150 N. Raman measurements were obtained from the sample surface at each tensile load, with the polarization direction of the Raman laser beam aligned parallel to the applied tensile stress.

MD Simulation: The large-scale atomic/molecular massively parallel simulator (LAMMPS) software is widely used for simulating and calculating the mechanical properties of various materials. Therefore, LAMMPS was employed to simulate the evolution of stress–strain under tensile and shear loading conditions for 4H-SiC crystals. This simulation is pivotal for determining the elastic modulus tensor values of 4H-SiC crystals across a range of temperatures. During the MD simulations, the lattice parameters for the initial unstressed crystal lattice of 4H-SiC were defined as follows: $a = b = 3.073$ Å and $c = 10.053$ Å.[53] The crystallographic orientations designated as [1−100], [11−20], and [0001] corresponded to the X-, Y-, and Z-axis, respectively. The dimensions of the model were delineated as 18.438 Å × 12.292 Å × 20.106 Å. Periodic boundary conditions were applied along all three spatial directions (X, Y, and Z axes) to circumvent boundary effects. Simulations were performed with a time step of 0.001 ps. Subsequently, the conjugate gradient algorithm was used to moderate the system towards a state of local minimum energy. After optimization, the 4H-SiC crystal model was subjected to uniaxial tensile or shear strains, operating at a strain rate of 10^9 s^{-1}. Temperature settings for the simulations ranged from 30 °C to 530 °C with increments of 50 °C. During uniaxial tensile deformation along the X-axis, the pressure in the perpendicular directions (Y and Z) was maintained at a nullified normal pressure. Similarly, for uniaxial tensile deformation along the Z axis, the pressures in the X- and Y-directions were restrained to a nullified normal pressure. During the shear deformation experiments, the normal pressures in all three directions (X, Y, and Z) were nullified to ensure that the deformation was purely shear. The derived stress–strain relationship from the simulations can facilitate the calculation of the elastic modulus tensor within the linear elastic regime.

FEM Simulation: The FEM simulations were performed using COMSOL Multiphysics 6.0 software. The dimensions of the 4H-SiC crystals used in the simulations were 10 mm × 10 mm × 0.362 mm, 5 mm × 5 mm × 0.362 mm, 4 mm × 4 mm × 0.362 mm, and 3 mm × 3 mm × 0.362 mm. The solid mechanical parameters were anisotropic, and the elastic modulus tensor values were directly derived from MD calculations. The simulation scope included a temperature range of 30–530 °C. Furthermore, the linear expansion coefficients for the simulations can be expressed as follows:[54]

$$\alpha_{11} = \alpha_{22} = 3.21 \times 10^{-6} + 3.56 \times 10^{-9} T - 1.62 \times 10^{-12} T^2$$
$$\alpha_{33} = 3.09 \times 10^{-6} + 2.63 \times 10^{-9} T - 1.08 \times 10^{-12} T^2 \quad (10)$$

Supporting Information

Supporting Information is available from the Wiley Online Library or from the author.

Acknowledgements

This work was partially supported by the National Natural Science Foundation of China (52275559), the Merit-based Zhejiang Province Postdoctoral Research Project (ZJ2023118), the Shanghai Synchrotron Radiation Facility, Beamline BL15U1 (proposal 2023-SSRF-PT-502316), and the Guangdong Basic and Applied Basic Research Foundation (No. 2023B1515120059). A Chat Generative Pre-Trained Transformer (ChatGPT, OpanAI) was used for language assistance.

Conflict of Interest

The authors declare no conflict of interest.

Data Availability Statement

The data that support the findings of this study are available from the corresponding author upon reasonable request.

Keywords

4H-SiC, in situ characterization, Raman shift–stress relationship, Raman spectroscopy, stress detection, temperature correction factor

Received: July 4, 2024
Revised: September 15, 2024
Published online:

[1] A. Itoh, H. Akita, T. Kimoto, H. Matsunami, *Appl. Phys. Lett.* **1994**, *65*, 1400.
[2] T. Kimoto, *Jpn. J. Appl. Phys.* **2015**, *54*, 040103.
[3] A. O. Konstantinov, Q. Wahab, N. Nordell, U. Lindefelt, *Appl. Phys. Lett.* **1997**, *71*, 90.
[4] W. J. Schaffer, G. H. Negley, K. G. Irvine, J. W. Palmour, *MRS Online Proc. Libr.* **2011**, *339*, 595.
[5] J. Ben Messaoud, J.-F. Michaud, D. Certon, M. Camarda, N. Piluso, L. Colin, F. Barcella, D. Alquier, *Micromachines* **2019**, *10*, 801.
[6] Y. Deng, Y. Zhou, Y. Zhang, *Exp. Mech.* **2022**, *62*, 1217.
[7] B. Matthey, T. Pirling, M. Herrmann, J. Schreiber, *J. Eur. Ceram. Soc.* **2020**, *40*, 1035.
[8] M. Mehregany, T. Lijun, L. G. Matus, D. J. Larkin, *IEEE Trans. Electron Devices* **1997**, *44*, 74.

[9] T. Nakano, N. Shinagawa, M. Yabu, N. Ohtani, *J. Cryst. Growth* **2019**, *516*, 51.
[10] Y.-J. Yu, D.-S. Byeon, Y.-J. Shin, S.-H. Choi, M.-H. Lee, W.-J. Lee, S.-M. Jeong, *CrystEngComm* **2017**, *19*, 6731.
[11] H. Xu, C. Wan, L. Sang, J.-P. Ao, *J. Cryst. Growth* **2019**, *505*, 59.
[12] L. Ma, W. Qiu, X. Fan, *Microelectron. Reliab.* **2021**, *118*, 114045.
[13] I. Latka, S. Dochow, C. Krafft, B. Dietzek, J. Popp, *Laser Photonics Rev.* **2013**, *7*, 698.
[14] N. Sugiyama, M. Yamada, Y. Urakami, M. Kobayashi, T. Masuda, K. Nishikawa, F. Hirose, S. Onda, *MRS Online Proc. Libr.* **2014**, *1693*, mrss14.
[15] J. Zhang, T. Liang, Y. Lu, B. Xu, T. Deng, Y. Zhang, Z. Zeng, X. Pi, D. Yang, R. Wang, *New J. Phys.* **2022**, *24*, 113015.
[16] M. Yoshikawa, K. Kosaka, H. Seki, T. Kimoto, *Appl. Spectrosc.* **2016**, *70*, 1209.
[17] H. Sakakima, S. Takamoto, Y. Murakami, A. Hatano, A. Goryu, K. Hirohata, S. Izumi, *Jpn. J. Appl. Phys.* **2018**, *57*, 106602.
[18] Z. Yang, X. Wang, W. Chen, H. Tang, R. Zhang, X. Fan, G. Zhang, J. Fan, *Laser Photonics Rev.* **2024**, *18*, 2301300.
[19] X. Zhou, H. Su, R. Yue, G. Dai, J. Li, Y. Wang, Z. Yu, *IEEE Trans. Power Electron.* **2018**, *33*, 5251.
[20] H. Sakakima, A. Goryu, A. Kano, A. Hatano, K. Hirohata, S. Izumi, *J. Appl. Phys.* **2020**, *128*, 025701.
[21] L. Anoldo, E. Zanetti, W. Coco, A. Russo, P. Fiorenza, F. Roccaforte, *Materials* **2024**, *17*, 1908.
[22] M. Bauer, A. M. Gigler, A. J. Huber, R. Hillenbrand, R. W. Stark, *J. Raman Spectrosc.* **2009**, *40*, 1867.
[23] M. Balkanski, R. F. Wallis, E. Haro, *Phys. Rev. B* **1983**, *28*, 1928.
[24] T. Kociniewski, J. Moussodji, Z. Khatir, *Microelectron. Reliab.* **2015**, *55*, 547.
[25] R. Sugie, T. Uchida, *J. Appl. Phys.* **2017**, *122*, 195703.
[26] A. Arora, A. Pandey, A. Patel, S. Dalal, B. S. Yadav, A. Goyal, R. Raman, O. P. Thakur, R. Tyagi, *J. Mater. Sci.: Mater. Electron.* **2020**, *31*, 16343.
[27] G. Kumar, J.-W. Chen, H.-H. Ma, X.-F. Huang, M. H. Huang, *J. Mater. Chem. C* **2022**, *10*, 10424.
[28] S. M. Lee, Y. Jang, J. Jung, J. H. Yum, E. S. Larsen, S. Y. Lee, H. Seo, C. W. Bielawski, H.-D. Lee, J. Oh, *ACS Appl. Electron. Mater.* **2019**, *1*, 617.
[29] C. Wang, A. Yi, P. Zheng, J. Lin, C. Shen, S. Zhang, K. Huang, X. Zhao, T. You, M. Zhou, J. Zhang, X. Ou, *Opt. Mater.* **2021**, *115*, 111068.
[30] J. McKenna, J. Patel, S. Mitra, N. Soin, V. Švrček, P. Maguire, D. Mariotti, *Eur. Phys. J. Appl. Phys.* **2011**, *56*, 24020.
[31] M. Rosso, A. Arafat, K. Schroën, M. Giesbers, C. S. Roper, R. Maboudian, H. Zuilhof, *Langmuir* **2008**, *24*, 4007.
[32] I. P. Vali, P. K. Shetty, M. G. Mahesha, V. G. Sathe, D. M. Phase, R. J. Choudhary, *Nucl. Instrum. Methods Phys. Res., Sect. B* **2019**, *440*, 101.
[33] H. Y. Sun, S.-C. Lien, Z. R. Qiu, H. C. Wang, T. Mei, C. W. Liu, Z. C. Feng, *Opt. Express* **2013**, *21*, 26475.
[34] G.-S. Sun, X.-F. Liu, H.-L. Wu, G.-G. Yan, L. Dong, L. Zheng, W.-S. Zhao, L. Wang, Y.-P. Zeng, X.-G. Li, Z.-G. Wang, *Chin. Phys. B* **2011**, *20*, 033301.
[35] H.-C. Wang, Y.-T. He, H.-Y. Sun, Z.-R. Qiu, D. Xie, T. Mei, C. C. Tin, Z.-C. Feng, *Chin. Phys. Lett.* **2015**, *32*, 047801.
[36] C. Rani, M. Tanwar, T. Ghosh, S. Kandpal, S. K. Saxena, R. Kumar, *Phys. Rep.* **2023**, *1037*, 1.
[37] H. F. Liu, N. Xiang, S. Tripathy, S. J. Chua, *J. Appl. Phys.* **2006**, *99*, 103503.
[38] F. Yan, H. Gao, H. Zhang, G. Wang, F. Yang, J. Yan, J. Wang, Y. Zeng, J. Li, *J. Appl. Phys.* **2007**, *101*, 023506.
[39] M. B. Bebek, C. M. Stanley, T. M. Gibbons, S. K. Estreicher, *Sci. Rep.* **2016**, *6*, 32150.
[40] S. K. Estreicher, T. M. Gibbons, B. Kang, M. B. Bebek, *J. Appl. Phys.* **2014**, *115*, 012012.
[41] Y. Wang, H. Dai, Z. Liu, D. Liu, *J. Phys. Chem. C* **2023**, *127*, 1109.
[42] X. L. Yang, X. F. Chen, Y. Peng, X. J. Xie, X. B. Hu, X. G. Xu, P. Yu, R. P. Wang, *Mater. Sci. Forum* **2017**, *897*, 307.
[43] Z. Tao, Y. Song, L. Zhang, Z. Xu, *Ceram. Int.* **2023**, *49*, 14190.
[44] M. Amilusik, D. Wlodarczyk, A. Suchocki, M. Bockowski, *Jpn. J. Appl. Phys.* **2019**, *58*, SCCB32.
[45] X. Qin, X. Li, X. Chen, X. Yang, F. Zhang, X. Xu, X. Hu, Y. Peng, P. Yu, *J. Alloys Compd.* **2019**, *776*, 1048.
[46] W. Li, H. Kou, X. Zhang, J. Ma, Y. Li, P. Geng, X. Wu, L. Chen, D. Fang, *Mech. Mater.* **2019**, *139*, 103194.
[47] X. Rao, F. Zhang, X. Luo, F. Ding, *Mater. Sci. Eng., A* **2019**, *744*, 426.
[48] M. Iuga, G. Steinle-Neumann, J. Meinhardt, *Eur. Phys. J. B* **2007**, *58*, 127.
[49] L. Pizzagalli, *Acta Mater.* **2014**, *78*, 236.
[50] W.-W. Xu, F. Xia, L. Chen, M. Wu, T. Gang, Y. Huang, *J. Alloys Compd.* **2018**, *768*, 722.
[51] J. Chen, A. Fahim, J. C. Suhling, R. C. Jaeger, in *2019 18th IEEE Intersociety Conf. on Thermal and Thermomechanical Phenomena in Electronic Systems (ITHERM)*, IEEE, Piscataway, NJ **2019**, pp. 835–840.
[52] W. Yuan, Y. Pei, Y. Li, N. Guo, X. Zhang, X. Liu, *Micromachines* **2024**, *15*, 600.
[53] G. L. Zhao, D. Bagayoko, *New J. Phys.* **2000**, *2*, 16.
[54] Z. Li, R. C. Bradt, *J. Appl. Phys.* **1986**, *60*, 612.